

1 DOI: 10.1002/((please add manuscript number))

2 **Article type: Communication**

3

4

5 **Anti-Pulverization Electrode Based on Low-Carbon Triple-Shelled**  
6 **Superstructures for Lithium-Ion Batteries**

7

8 *Lianhai Zu, Qingmei Su, Feng Zhu, Bingjie Chen, Huanhuan Lu, Chengxin Peng, Ting He,*

9 *Gaohui Du, Pengfei He, Kai Chen, Shihe Yang, Jinhua Yang\* and Huisheng Peng\**

10

11 Dr. L. H. Zu, B. J. Chen, C. X. Peng and Prof. J. H. Yang

12 School of Chemical Science and Engineering, Tongji University, Shanghai 200092, China.

13 E-mail: yangjinhua@tongji.edu.cn

14 L. H. Zu and Prof. J. H. Yang

15 Research Center for Translational Medicine & Key Laboratory of Arrhythmias of the Ministry

16 of Education of China, East Hospital, Tongji University School of Medicine, No. 150 Jimo

17 Road, Shanghai 200120, P. R. China

18 Dr. Q. M. Su and Prof. G. H. Du

This is the author manuscript accepted for publication and has undergone full peer review but has not been through the copyediting, typesetting, pagination and proofreading process, which may lead to differences between this version and the [Version of Record](#). Please cite this article as [doi: 10.1002/adma.201701494](https://doi.org/10.1002/adma.201701494).

This article is protected by copyright. All rights reserved.

1 Institute of Physical Chemistry, Zhejiang Normal University, Jinhua 321004, P. R. China.

2 Dr. F. Zhu and Prof. P. F. He

3 School of Aerospace Engineering and Applied Mechanics, Tongji University, Shanghai

4 200433, China

5 Prof. H. S. Peng

6 State Key Laboratory of Molecular Engineering of Polymers, Department of Macromolecular

7 Science and Laboratory of Advanced Materials, Fudan University, Shanghai 200433, China.

8 Dr. T. He

9 School of Materials Science and Engineering, Tongji University, Shanghai 201804, China.

10 H. H. Lu and Prof. Kai Chen

11 Center for Advancing Materials Performance from the Nanoscale (CAMP-Nano), State Key

12 Laboratory for Mechanical Behavior of Materials, Xi'an Jiaotong University, Xi'an, China

13 Prof. S. H. Yang

14 Department of Chemistry, The Hong Kong University of Science and Technology, Clear

15 Water Bay, Kowloon, Hong Kong, China.

16 E-mail: penghs@fudan.edu.cn

17

18 Keywords: SnO<sub>2</sub>, carbon, anti-pulverization, triple-shelled structure, lithium-ion battery

19

1       **Abstract:** The realization of anti-pulverization electrode structures, especially using low-carbon-  
2       content anode materials, is crucial for developing high-energy and long-life lithium-ion batteries  
3       (LIBs); however, this technology remains challenging. Here, we show that SnO<sub>2</sub> triple-shelled hollow  
4       superstructures (TSHSs) with a low carbon content (4.83%) constructed by layer-by-layer assembly of  
5       various nanostructure units can withstand a huge volume expansion of ~231.8% and deliver a high  
6       reversible capacity of 1099 mAh g<sup>-1</sup> even after 1450 cycles. These values represent the best  
7       comprehensive performance in SnO<sub>2</sub>-based anodes to date. Mechanics simulations and *in situ*  
8       transmission electron microscopy suggest that the TSHSs enable a self-synergistic structure-  
9       preservation behavior upon lithiation/delithiation, protecting the superstructures from collapse and  
10      guaranteeing the electrode structural integrity during long-term cycling. Specifically, the outer shells  
11      during lithiation processes are fully lithiated, preventing the overlithiation and the collapse of the inner  
12      shells; in turn, in delithiation processes, the underlithiated inner shells work as robust cores to support  
13      the huge volume contraction of the outer shells; meanwhile, the middle shells with abundant pores  
14      offer sufficient space to accommodate the volume change from the outer shell during both lithiation  
15      and delithiation. This study opens a new avenue in the development of high-performance LIBs for  
16      practical energy applications.

17  
18      As one of the current major energy storage technologies, lithium-ion batteries (LIBs) are  
19      widely expected to power emerging portable electronics and electric vehicles (EVs)<sup>1-4</sup>. To  
20      meet demand, it is necessary to develop high-energy-density LIBs with both long cycling life  
21      and high power output. However, LIBs have long suffered from the severe pulverization of  
22      anode materials induced by huge volume changes upon Li ion insertion/extraction, which  
23      causes irreversible capacity loss as well as poor cycling stability and rate capability<sup>5-17</sup>. To  
24      solve this problem, in most cases, graphitic carbons with good conductivity and excellent  
25      mechanical properties were employed as flexible matrices for the anode materials to  
26      improve the cycling performance of batteries<sup>18-29</sup>. However, the high carbon content (usually

This article is protected by copyright. All rights reserved.

1 greater than 30%) often results in a capacity decrease due to the low theoretical lithium  
2 storage capacity of graphite carbons ( $\sim 372 \text{ mAh g}^{-1}$ ), substantially limiting their practical  
3 applications in EVs. One effective way to elevate energy density is to reduce the carbon  
4 content in composite anode materials. Nevertheless, it remains a considerable challenge to  
5 produce such composite materials with sufficiently low carbon content to ensure high  
6 capacity and, simultaneously, maintain a stable architecture for long cycling life.

7  $\text{SnO}_2$  is an attractive anode material for LIBs due to its high theoretical lithium storage  
8 capacity ( $\sim 782 \text{ mA g}^{-1}$ ) and safe working potential ( $\sim 0.6 \text{ V vs. Li}^+/\text{Li}$ )<sup>17,30,31,32-35</sup>. However,  
9  $\text{SnO}_2$  also suffers from a large volume change ( $\sim 250\%$ ) and severe structural collapse that  
10 result in an unstable solid electrolyte interphase (SEI)<sup>36</sup> and an overall performance  
11 deterioration of batteries. To date,  $\text{SnO}_2$ -based batteries capable of delivering a high  
12 reversible capacity ( $> 800 \text{ mAh g}^{-1}$ ) over 1000 cycles have been extremely limited. In this  
13 regard,  $\text{SnO}_2$  represents a typical class of LIB anode material facing a serious structural  
14 collapse problem that still requires resolution. Therefore,  $\text{SnO}_2$  was selected as an example  
15 for investigation. In this work,  $\text{SnO}_2$  triple-shelled hollow superstructures (TSHSs) with low

1 carbon content (4.83%) assembled hierarchically using various SnO<sub>2</sub>-based primary  
2 nanostructure units show high lithium storage performance, including a high reversible  
3 capacity (1099 mAh g<sup>-1</sup>) at 0.5 A g<sup>-1</sup> with a high capacity retention of nearly 100% after 1450  
4 cycles and a high power output (416 mAh g<sup>-1</sup> at 4A g<sup>-1</sup>) with long cycle life (1200 cycles).  
5 Further mechanics simulations coupled with *in situ* transmission electron microscopy (TEM)  
6 suggest that such a triple-shelled configuration enables a self-synergistic structure-  
7 preservation (SSSP) behavior upon lithiation/delithiation, protecting the TSHSs against  
8 collapse and guaranteeing electrode structural integrity during cycling. Therefore, the  
9 superior performance of the SnO<sub>2</sub> TSHS is attributed to the following two factors: the optimal  
10 structural/composition design of the TSHSs that favors the generation of high-performance  
11 LIBs and the SSSP behavior that maintains the structural integrity of the TSHSs throughout  
12 the lithiation/delithiation process. The SSSP concept provides a new strategy to construct  
13 anti-pulverization electrodes for high-performance LIBs based on low-carbon-content or  
14 carbon-free anode materials.

This article is protected by copyright. All rights reserved.

1 The synthesis of the TSHSs was realized through the layer-by-layer growth/assembly of  
2 various SnO<sub>2</sub> nanounits on the surface of SiO<sub>2</sub> nanospheres, coupled with  
3 carbonization/coating of carbon precursors. As shown in Figure 1a, the rapid hydrolysis of  
4 Na<sub>2</sub>SnO<sub>3</sub>·3H<sub>2</sub>O in an ethanol-water solution leads to the dense deposition of SnO<sub>2</sub> nanodots  
5 on SiO<sub>2</sub> nanospheres, forming the first shell of SnO<sub>2</sub> nanodots (Figure 1a, step ①).  
6 Subsequently, the synchronous hydrolysis of the Sn-precursor and  
7 polymerization/carbonization of glucose induce the formation of organic carbon (OC)-coated  
8 SnO<sub>2</sub> nanodots and their loosely assembled second layer on the surface of the first dense  
9 layer (step ②). The double-shelled intermediates, when calcined under N<sub>2</sub> atmosphere for  
10 complete carbonization after removing the SiO<sub>2</sub> cores using NaOH solution, transform into  
11 the SnO<sub>2</sub> double-shelled hollow superstructures (DSHSs) (Figure 1a, step ③). The double-  
12 layer intermediates with exposed OH-rich groups then serve as hydrophilic interfaces for  
13 further seeded growth of SnO<sub>2</sub> nanorods, forming the third layer made of radially arrayed  
14 nanorods (Figure 1a, step ④). Finally, after deposition of graphenized carbon by chemical  
15 vapor deposition in C<sub>2</sub>H<sub>2</sub> flow, the SnO<sub>2</sub> TSHSs are produced (Figure 1a, step ⑤). In the

1 following sections, SnO<sub>2</sub> DSHSs were selected and examined together with the SnO<sub>2</sub>  
2 TSHSs for comparison, to better understand the role of the triple-shelled configuration of the  
3 SnO<sub>2</sub> TSHSs in the structural stability and battery performance.

4 The structural and elemental analyses of the SnO<sub>2</sub> DSHSs and TSHSs were conducted in  
5 detail. A scanning electron microscopy (SEM) image in Figure 1b shows that the SnO<sub>2</sub>  
6 DSHSs are monodisperse with rougher surfaces and larger sizes (~480 nm) relative to the  
7 pristine SiO<sub>2</sub> nanospheres (d = 300 nm, Figure S1). From the TEM image (Figure 1c), it can  
8 be seen that the SnO<sub>2</sub> DSHSs are hollow with double shells, namely, a dense inner shell  
9 (the first shell) and a loose outer shell (the second shell). As shown in Figure 1d, there is a  
10 clear boundary between the two shells. The first shell is ~25 nm thick, made of densely  
11 aggregated SnO<sub>2</sub> nanodots, whereas the second shell possesses a larger shell thickness of  
12 ~60 nm, consisting of loosely packed SnO<sub>2</sub>@C nanodots. A high-resolution TEM image  
13 (Figure 1d, inset) indicates that the SnO<sub>2</sub> nanodots are coated with a few layers of  
14 graphenized carbon. In addition, clear crystal lattices with a d-spacing of 0.335 nm were  
15 observed, corresponding to the (110) plane of the tetragonal crystal structure of SnO<sub>2</sub>

1 (JCPDS no. 70-4177). The carbon coating on the SnO<sub>2</sub> nanodots leads to the loose packing  
2 of the SnO<sub>2</sub>@C nanodots and the formation of the thicker second shells. Compared to the  
3 SnO<sub>2</sub> DSHSs, the SnO<sub>2</sub> TSHSs exhibit much rougher surfaces and larger sizes of ~700 nm  
4 after the growth of the third shell of nanorod arrays, as shown in Figure 1e. The hollow  
5 characteristics and triple-shelled configuration are further revealed by the TEM image in  
6 Figure 1f. The second shells give a relatively lower contrast compared with the other two  
7 shells, caused by the lower stacking density of the SnO<sub>2</sub>@C nanodots. The triple-shelled  
8 configuration can be clearly observed in a selected-area TEM image in Figure 1g; the image  
9 shows that the third shell is made of densely assembled SnO<sub>2</sub> nanorods, with a shell  
10 thickness of ~110 nm (Figure 1g, inset at the bottom). The nanorods are estimated to be ~3-  
11 5 nm in diameter and are coated with a few layers (2-3) of graphenized carbon, as judged  
12 from the corresponding high-magnification TEM image (Figure 1g and inset on the top).

13 The presence of C, O and Sn elements in the SnO<sub>2</sub> TSHSs is evidenced by the  
14 corresponding element maps and EDS analysis (Figure S2a and 2b). Line scanning of the  
15 TSHS illustrates a shell-dependent distribution of the three elements (Figure S2c and 2d),

1 confirming the triple-shelled configuration of the TSHS. The XRD patterns indicate that  
2 DSHSs and TSHSs are both in tetragonal crystal structure (JCPDS no. 70-4177) (Figures  
3 S3a and S4a). The BET measurements reveal the presence of hierarchical pores, namely,  
4 micropores with diameters of ~3.5 nm and macropores of ~250 nm (hollow interiors) in the  
5 SnO<sub>2</sub> DSHSs and TSHSs (Figures S3b and S4b). The BET surface areas for the SnO<sub>2</sub>  
6 DSHSs and TSHSs are 149.3 and 65.8 m<sup>2</sup> g<sup>-1</sup>, respectively. The Raman spectra in Figures  
7 S3c and S4c show typical D and G peaks for graphene materials<sup>37,38</sup>, implying that the  
8 carbon contained in the samples is graphenized. It is noted that the carbon content in the  
9 SnO<sub>2</sub> TSHSs is relatively low (4.83%, mass ratio) compared to that of the SnO<sub>2</sub> DSHSs  
10 (35.1%) and other previously reported SnO<sub>2</sub>-C composites (Table S1)<sup>26,27,33,39-46</sup>. Therefore,  
11 with a set of structural/compositional advantages, such as a high content of SnO<sub>2</sub> active  
12 materials (95.17%), a relative high specific surface area (65.8 m<sup>2</sup> g<sup>-1</sup>) and hierarchical pores,  
13 the TSHSs are expected to be a promising anode material for creating high-performance  
14 LIBs.

1 Figure 2 shows the electrochemical performance of the two electrodes based on the SnO<sub>2</sub>  
2 DSHSs and TSHSs. The long-term cycling tests measured at a current density of 0.5 A g<sup>-1</sup>  
3 over the voltage range of 0.05~2.5 V are shown in Figure 2a. It can be seen that the SnO<sub>2</sub>  
4 TSHS electrode displays much higher specific capacities than the DSHS electrode  
5 throughout the cycling. For example, in the first cycle, the SnO<sub>2</sub> TSHS electrode delivers a  
6 higher discharge capacity of 2050 mAh g<sup>-1</sup> as well as a higher initial Coulombic efficiency of  
7 51.2% (Figure S5) relative to the SnO<sub>2</sub> DSHS electrode (1627 mAh g<sup>-1</sup>, 44.1%). It is noted  
8 that the discharge capacities are two times the theoretical value (~782 mAh g<sup>-1</sup>) of SnO<sub>2</sub>  
9 material, attributed to the decomposition of the electrolyte forming a solid electrolyte  
10 interface (SEI) film<sup>36,47</sup>. The SnO<sub>2</sub> TSHS electrode shows an upward trend in capacity upon  
11 cycling accompanied by a slight fluctuation. The high capacities above 750 mAh g<sup>-1</sup> are  
12 delivered during the entire cycling process. Notably, a capacity of ~1099 mAh g<sup>-1</sup> is  
13 maintained after 1450 cycles, corresponding to a high capacity retention of ~104.7%. For the  
14 SnO<sub>2</sub> DSHS electrode, however, a constant capacity decrease occurred throughout the  
15 cycling process, resulting in a low capacity of 155 mAh g<sup>-1</sup> and a low capacity retention of

This article is protected by copyright. All rights reserved.

1 21.6% after cycling, only ~14.3% and ~20% of the SnO<sub>2</sub> TSHS electrode values,  
2 respectively. The trend in capacity change is reflected in the galvanostatic charge/discharge  
3 profiles of the SnO<sub>2</sub> TSHS electrode (Figure 2b). Moreover, at higher current densities of 1  
4 and 2 A g<sup>-1</sup>, the TSHS electrode can also deliver high capacities almost twice those of the  
5 DSHS electrode (Figure S6).

6 In addition, the SnO<sub>2</sub> TSHS electrode manifests a remarkable rate capability compared to  
7 the DSHS electrode. As shown in Figure 2c and Table S2, the SnO<sub>2</sub> TSHS electrode  
8 demonstrates high reversible capacities, from ~931 mAh g<sup>-1</sup> at 0.2 A g<sup>-1</sup> to 120 mAh g<sup>-1</sup> at 16  
9 A g<sup>-1</sup>, which is approximately 34%~344% higher than those of the SnO<sub>2</sub> DSHS electrode.  
10 Moreover, when the current density returns from 16 A g<sup>-1</sup> to the initial 0.2 A g<sup>-1</sup> after 120  
11 cycles, the SnO<sub>2</sub> TSHS electrode still delivers a high capacity of 872 mAh g<sup>-1</sup>, with a capacity  
12 retention of ~93.7%. The outstanding rate capability of the SnO<sub>2</sub> TSHS electrode is also  
13 confirmed by the voltage profiles tested at the corresponding current densities (Figure 2d).  
14 Moreover, to further evaluate the long-cycle high-power performance, long-term cycling tests  
15 (up to 1200 cycles) at a high current density of 4 A g<sup>-1</sup> were applied to the two electrodes. It

1 can be seen in Figure S7 that the SnO<sub>2</sub> TSHS electrode is generally stable during the  
2 cycling and displays an upward trend in capacity in the latter 1000 cycles from the 200th to  
3 the 1200th cycle. The capacity finally stabilizes at 416 mAh g<sup>-1</sup> with a capacity retention of  
4 57.5% after 1200 cycles, which far surpasses the remaining capacity (123 mAh g<sup>-1</sup>) for the  
5 SnO<sub>2</sub> DSHS electrode, as well as its corresponding capacity retention (25.7%). To the best  
6 of our knowledge, the superior performance of the SnO<sub>2</sub> TSHS electrode, such as the  
7 ultrahigh capacity (1099 mAh g<sup>-1</sup> at 0.5 A g<sup>-1</sup>) remaining after long-term cycling (1450 cycles),  
8 with a capacity retention of nearly 100%, and its high power output (416 mAh g<sup>-1</sup> at 4A g<sup>-1</sup>)  
9 with long cycle life (1200 cycles), is among the best comprehensive performances for SnO<sub>2</sub>-  
10 based anode materials reported so far. Performance comparisons between the LIBs based  
11 on the SnO<sub>2</sub> TSHSs and other SnO<sub>2</sub> anode materials are provided in Figure 2e and Table S1.  
12 In addition, it is found that the high capacity uptake of the SnO<sub>2</sub> TSHSs are derived from  
13 their triple-shelled configuration that enables higher reaction reversibility with a higher  
14 theoretical capacity, which is analyzed and discussed in detail based on cyclic voltammetry  
15 (CV) studies (S1, S2, Figures S8-S13)<sup>48-51</sup>.

1 It is found that the TSHSs can withstand huge volume change upon lithiation/delithiation  
2 after even 1450 cycles, whereas the DSHSs fail. Unlike the stable SEI film formed on the  
3 TSHSs, the collapse process of the DSHSs induces repeated formation of new SEI films  
4 around the surface of DSHS fragments, leading to unstable lithiation/delithiation interfaces,  
5 as illustrated in Figure 3a. Figure 3b shows the TEM images of the TSHSs undergoing  
6 lithiation/delithiation for 1450 cycles. It can be seen that the morphology of the TSHSs is  
7 preserved well (Figure 3b, inset, and Figure S14), with a thin SEI film ( $\sim 20$  nm) covering the  
8 surface of the outer shell. The existence of SEI films for the TSHSs and DSHSs are  
9 confirmed by XPS analyses shown in Figure S15 and Figure S16, where some typical XPS  
10 peaks correspond to LiF,  $\text{PF}_6^-$  and C=O bonds that are generally considered as the main  
11 compositions of SEI film formed from the decomposition of the electrolyte of  $\text{LiPF}_6$ . At a high  
12 magnification, it is seen that the outer shells consist of uniform nanodots, indicating that the  
13 nanorods in the outer shell have turned into ultrasmall nanodots after the long-term cycling.  
14 Some  $\text{SnO}_2$  nanodots with crystalline domains of  $\sim 2\text{-}4$  nm are observed in the outer shell,  
15 without an SEI film existing on the nanodot surfaces (Figure 3c). By contrast, the DSHS is

This article is protected by copyright. All rights reserved.

1 collapsed into pieces with cracks during cycling (Figure 3d and Figure S14); the new  
2 surfaces of the fragments generated during the collapse process are coated with abundant  
3 SEI film. The collapse of the DSHSs leads to the pulverization of the DSHS electrode, which  
4 inevitably induces the direct loss of active materials and an unstable SEI film repeatedly  
5 being formed at newly generated interfaces, thus resulting in a capacity decrease and  
6 cycling instability<sup>7,52</sup>.

7 *In situ* TEM was employed to monitor the real-time structural evolution of the TSHS and  
8 DSHS electrodes during a lithiation/delithiation cycle. The setup for the *in situ* TEM device is  
9 illustrated in Figure 3f, where a selected TSHS or DSHS connected to the Au tip serves as a  
10 working electrode and a piece of Li coated with Li<sub>2</sub>O on W nanowire tip works as a counter  
11 electrode. As shown in Figure 3g and movie S1, the TSHS expands immediately after  
12 application of voltage bias. The radius of the TSHS increases gradually from the initial 360  
13 nm to the maximum of 468 nm after 350 s of Li deposition and then shrinks to the minimum  
14 367 nm after another 110 s of Li extraction. It is noted that the hollow interior also undergoes  
15 an “expansion/contraction” process in response to lithiation/delithiation, implying a

This article is protected by copyright. All rights reserved.

1 synchronous expansion/contraction behavior of the three shells. It can also be found that  
2 some nanorods in the outer shell transform into smaller nanodots after the cycle, and the  
3 triple-shelled configuration of the TSHS is still well preserved. For the DSHS, it collapsed in  
4 5 s during the volume shrinking process after 150 s of volume expansion with the radius  
5 increasing from 254 nm to 310 nm (Figure 3h and Movie S2). Some key values, such as  
6 volume changes as well as volume expansion ratios during lithiation for each shell of the  
7 DSHS and TSHS, were calculated (S3) and are listed in Table S3, in terms of the data  
8 obtained from *in situ* TEM observation. As can be seen, the first, second and third shells for  
9 the TSHS expanded to 145.1%, 187.9% and 242% (volume expansion ratio,  $r_{VV}$ ),  
10 respectively, with a general expansion ratio ( $R_{VV}$ ) of 231.8%. Relatively, the DSHS has a  
11 higher  $r_{VV}$  of 157.4% and 208.6% in the first shell and second shell, respectively, but a lower  
12  $R_{VV}$  of 188.1%. Theoretically, the volume expansion ratio is proportional to the extent of  
13 lithiation, and a higher volume expansion ratio corresponds to a higher lithiation degree with  
14 a higher capacity. As a consequence, the TSHS can deliver higher reversible capacities  
15 (Figure 2c), due to its higher general volume expansion ratio (231.8%) than that (188.1%) of

This article is protected by copyright. All rights reserved.

1 the DSHS, which even approaches the theoretical value of 250%<sup>49,50</sup>. In addition, the  
2 existence of the third shell in TSHSs can reduce the lithiation extent of both the first shell  
3 (145.1% vs 157.4%) and the second shell (187.9% vs 208.6%), thereby preventing the  
4 collapse of the two shells as well as the TSHSs. Specifically, the third shell contributes  
5 ~92.57% capacity to the total, whereas the other two shells give less than 8%, according to  
6 the calculations on the capacity contribution ratio ( $R_{\Delta V/\Delta V}^i$ ) of individual shells for the TSHS.  
7 The calculations support quantitatively the electrochemical results that demonstrate that the  
8 TSHSs can uptake a higher capacity and are more stable against lithiation/delithiation.

9 It is still surprising that the triple-shelled configuration of the SnO<sub>2</sub> TSHSs, with a low  
10 carbon content of 4.83%, can withstand huge volume expansion of up to 242% after  
11 thousands of cycles. The test of *in situ* mechanical TEM on an individual TSHS was  
12 conducted (Figure S17). The load-displacement curve of a typical compression test on an  
13 individual TSHS shows that even with the formation of the crack, the loading force kept  
14 increasing, and the TSHS does not fracture or break into pieces as commonly observed in  
15 other cases, demonstrating an anti-pulverization structure of TSHS. To more deeply

This article is protected by copyright. All rights reserved.

1 understand why the TSHS is stable during the lithiation process, an elastic-plastic model  
2 coupled to Li diffusion was adopted to evaluate the lithiation-induced deformation and stress  
3 states (S4). In the simulations, we are more attentive to tensile stress as it is the key factor  
4 for the collapse of the electrode structures. Figure 4a shows the morphology evolution of  
5 TSHSs during the lithiation process, where colors from blue to red correspond to different  
6 lithiation extents (or Li-ion concentrations) from low lithiation to high lithiation, respectively.  
7 Initially, the Li-ion concentration in the TSHS structure is  $\sim 0$  (0 s). Afterwards, partial  
8 lithiation of the TSHS occurs, leading to some structural deformation on the side contacting  
9 the electrode (120 s). This deformation continues until the TSHS is fully lithiated at 350 s.  
10 The stress simulation after the lithiation in Figure 4b shows that the third shell experiences  
11 very low tensile stress, despite a huge compressive stress (up to  $\sim 230$  MPa) in the region  
12 adjacent to the second shell. The second shell is almost in a stress-free state due to the  
13 existence of sufficient inter-nanodot space to effectively relieve both tensile and compressive  
14 stress. For the first shell, a tensile stress ( $\sim 150$  MPa) generates dramatically near the region  
15 between the first and the second shells. Figure 4c presents the stress state for the TSHS at

This article is protected by copyright. All rights reserved.

1 different lithiation extents and times during the lithiation process. It can be found that a  
2 tensile stress exists in the first shell throughout the lithiation, with the corresponding peak  
3 values increasing monotonically with lithiation proceeding (Figure 4d). For the DSHS, a  
4 similar structural deformation occurred during lithiation, as shown in Figure S18a. However,  
5 the tensile stress behavior in the first shell during lithiation is different from that of the TSHS  
6 (Figure S18 b-d). As shown in Figure S18d, the peak values of the tensile stress decrease  
7 continuously through the lithiation process from ~185 MPa to ~110 MPa, which indicates that  
8 the DSHS may collapse at the very beginning of the lithiation process. It is noted that the  
9 DSHS undergoes a higher maximum tensile stress (~185 MPa) in the first shell than that  
10 (~165 MPa) of the TSHS, demonstrating that the TSHS possesses better structural stability  
11 due to the triple-shelled configuration.

12 It is noteworthy that the DSHS collapsed during volume shrinking, instead of volume  
13 expanding, in the delithiation process (Figure 3h, *in situ* TEM observation). This result  
14 implies that a high tensile stress should be produced during the delithiation process and lead  
15 to the collapse of the DSHS. The stress states for the sample, however, are challenging to

1 simulate due to the difficulty of modeling delithiation processes. For the TSHS, a huge  
2 tensile stress during the delithiation process is also considered to be generated, especially in  
3 the third shell, which is the most lithiated and expanded. As seen in Figure 3g, compared  
4 with the initial state before cycling, the space of the second shell of the TSHS after  
5 delithiation is clearly compressed, whereas the position of the first shell is almost unchanged  
6 (R1, from initial 180 nm to final 181 nm). This finding demonstrates that the third shell has  
7 experienced tremendous volume shrinkage and huge tensile stress that may transfer to the  
8 first shell via the second shell. The first shell is underlithiated in the lithiation process,  
9 observed from *in situ* high-resolution TEM images of the TSHS in Figure S19. The first shell  
10 with a low lithiation extent and a low volume change may serve as a robust and stable inner  
11 core to support the shrunken third shell and alleviate the stress in the third shell, protecting  
12 the third shell as well as the TSHS from collapse. Certainly, the second shell with abundant  
13 pores may also be crucial for buffering the volume shrinkage from the third shell.  
14 Consequently, the TSHS can effectively resist the huge volume contraction.

1 Taking both lithiation and delithiation into consideration, it can be deduced that a self-  
2 synergistic structure-preservation behavior occurs in the TSHSs during cycling: as illustrated  
3 in Figure S20a, during the lithiation process, the third shells that contribute to the major  
4 capacity prevent the overlithiation and the breaking of the first shells; in turn, in the  
5 delithiation process, the underlithiated first shells work as a robust core to support the huge  
6 volume contraction of the third shells; and the second shells with abundant pores offer  
7 sufficient space to accommodate the volume change from the third shell during both lithiation  
8 and delithiation<sup>55</sup>. By contrast, for the DSHS, without the third shells that consume most of  
9 the lithium ions released from the cathode, the first inner shells are fully lithiated with more  
10 volume expansion in the lithiation process, and subsequently undergo tremendous volume  
11 shrinkage and huge tensile stress during delithiation, which leads to the collapse of the first  
12 shells as well as the DSHSs (Figure S20b).

13 In summary, SnO<sub>2</sub> TSHSs were fabricated via the layer-by-layer assembly of various SnO<sub>2</sub>  
14 structure units. SnO<sub>2</sub> TSHSs exhibit outstanding lithium-storage performance as an LIB  
15 anode, such as high capacity, long cycling life and high rate capability. The superior

This article is protected by copyright. All rights reserved.

1 comprehensive performance is ascribed to the unique structural design of the TSHSs and  
2 the SSSP mechanism that maintains the structural integrity of the TSHSs during the  
3 lithiation/delithiation process. The SSSP behavior is derived from the triple-shelled  
4 configuration of the TSHSs, which is demonstrated by *in situ* TEM and mechanics  
5 simulations. This study establishes a prototypical model to recognize the specific working  
6 mechanism involved in the hollow or multi-shelled structure anodes that have been widely  
7 employed for LIBs. This novel SSSP concept provides a new strategy to construct anti-  
8 pulverization electrodes, using carbon-free anode materials or those containing less carbon,  
9 for the development of high-performance LIBs with high energy, long cycle life and high  
10 power.

11

## 12 References

13 [1] B. Dunn, H. Kamath, *Science* **2011**, 334, 928-935.

14 [2] B. Kang, G. Ceder, *Nature* **2009**, 458, 190-193.

This article is protected by copyright. All rights reserved.

- 1 [3] M. K. Song, S. Park, F. M. Alamgir, J. Cho, M. Liu, *Mater. Sci. Eng. Rep.* **2011**, *72*,  
2 203-252.
- 3 [4] M. Armand, J. M. Tarascon, *Nature* **2008**, *451*, 652-657.
- 4 [5] X. Li, M. Gu, S. Hu, R. Kennard, P. Yan, X. Chen, C. Wang, M. J. Sailor, J. G. Zhang,  
5 J. Liu, *Nat. Commun.* **2014**, *5*, 4105.
- 6 [6] J. Liu, P. Kopold, C. Wu, P. A. van Aken, J. Maier, Y. Yu, *Energy Environ. Sci.* **2015**, *8*,  
7 3531-3538.
- 8 [7] Y. Li, K. Yan, H. W. Lee, Z. Lu, N. Liu, Y. Cui, *Nature Energy* **2016**, *1*, 15029.
- 9 [8] J. Wang, H. Tang, L. Zhang, H. Ren, R. Yu, Q. Jin, J. Qi, D. Mao, M. Yang, Y. Wang,  
10 P. Liu, Y. Zhang, Y. Wen, L. Gu, G. Ma, Z. Su, Z. Tang, H. Zhao, D. Wang, *Nature*  
11 *Energy* **2016**, *1*, 16050.
- 12 [9] Z. Y. Wang, L. Zhou, X. W. Lou, *Adv. Mater.* **2012**, *24*, 1903-1911.
- 13 [10] Y. J. Hong, M. Y. Son, Y. C. Kang, *Adv. Mater.* **2013**, *25*, 2279-2283.

- 1 [11] N. Liu, Z. D. Lu, J. Zhao, M. T. McDowell, H. W. Lee, W. T. Zhao, Y. Cui, *Nature*  
2 *Nanotech.* **2014**, 9, 187-192.
- 3 [12] L. Zhou, D. Y. Zhao, X. W. Lou, *Adv. Mater.* **2012**, 24, 745-748.
- 4 [13] J. Liu, H. Xia, D. F. Xue, L. Lu, *J. Am. Chem. Soc.* **2009**, 131, 12086-12087.
- 5 [14] G. Q. Tan, F. Wu, Y. F. Yuan, R. J. Chen, T. Zhao, Y. Yao, J. Qian, J. R. Liu, Y. S. Ye,  
6 R. Shahbazian-Yassar, J. Lu, K. Amine, *Nature Commun.* **2016**, 7, 11774.
- 7 [15] M. J. Zhou, Y. C. Liu, J. Chen, X. L. Yang, *J. Mater. Chem. A* **2015**, 3, 1068-1076.
- 8 [16] W. W. Xu, K. N. Zhao, C. J. Niu, L. Zhang, Z. Y. Cai, C. H. Han, L. He, T. Shen, M. Y.  
9 Yan, L. B. Qu, L. Q. Mai, *Nano Energy* **2014**, 8, 196-204.
- 10 [17] S. Chen, M. Wang, J. F. Ye, J. G. Cai, Y. R. Ma, H. H. Zhou, L. M. Qi, *Nano Res.*  
11 **2013**, 6, 243-252.
- 12 [18] H. Liu, W. Li, D. Shen, D. Zhao, G. Wang, *J. Am. Chem. Soc.* **2015**, 137, 13161-  
13 13166.

- 1 [19] R. Y. Zhang, Y. J. Du, D. Li, D. K. Shen, J. P. Yang, Z. P. Guo, H. K. Liu, A. A.  
2 Elzafahry, D. Y. Zhao, *Adv. Mater.* **2014**, 26, 6749-6755.
- 3 [20] J. Liang, X.Y. Yu, H. Zhou, H. B. Wu, S. J. Ding, X. W. Lou, *Angew. Chem. Int. Ed.*  
4 **2014**, 53, 12803-12807.
- 5 [21] W. Ni, Y. B. Wang, R. Xu, *Part. Part. Syst. Charact.* **2013**, 30, 873-880.
- 6 [22] L. Zhang, H. B. Wu, B. Liu, X. W. Lou, *Energy Environ. Sci.* **2014**, 7, 1013-1017.
- 7 [23] R. Z. Hu, H. Y. Zhang, J. W. Liu, D. C. Chen, L. C. Yang, M. Zhu, M. L. Liu, *J. Mater.*  
8 *Chem. A* **2015**, 3, 15097-15107.
- 9 [24] S. M. Hwang, Y. G. Lim, J. G. Kim, Y. U. Heo, J. H. Lim, Y. Yamauchi, M. S. Park, Y.J.  
10 Kim, S. X. Dou, J. H. Kim, *Nano Energy* **2014**, 10, 53-62.
- 11 [25] L. Zhang, G. Q. Zhang, H. B. Wu, L. Yu, X. W. Lou, *Adv. Mater.* **2013**, 25, 2589-2593.
- 12 [26] D. N. Wang, J. L. Yang, X. F. Li, D. S. Geng, R. Li, M. Cai, T. K. Sham, X. L. Sun,  
13 *Energy Environ. Sci.* **2013**, 6, 2900-2906.

- 1 [27] S.H. Yu, D. J. Lee, M. Park, S. G. Kwon, H. S. Lee, A. Jin, K.S. Lee, J. E. Lee, M. H.  
2 Oh, K. Kang, Y.E. Sung, T. Hyeon, *J. Am. Chem. Soc.* **2015**, 137, 11954-11961.
- 3 [28] J. Qin, C. N. He, N. Q. Zhao, Z. Y. Wang, C. S. Shi, E. Z. Liu, J. J. Li, *ACS Nano* **2014**,  
4 8, 1728-1738.
- 5 [29] C. X. Peng, B. D. Chen, Y. Qin, S. H. Yang, C. Z. Li, Y. H. Zuo, S. Y. Liu, J. H. Yang,  
6 *ACS Nano* **2012**, 6, 1074-1081.
- 7 [30] X. W. Lou, C. M. Li, L. A. Archer, *Adv. Mater.* **2009**, 21, 2536-2539.
- 8 [31] C. Wang, Y. Zhou, M. Y. Ge, X. B. Xu, Z. L. Zhang, J. Z. Jiang, *J. Am. Chem. Soc.*  
9 **2010**, 132, 46-47.
- 10 [32] V. Aravindan, K. B. Jinesh, R. R. Prabhakar, V. S. Kale, S. Madhavi, *Nano Energy*  
11 **2013**, 2, 720-725.
- 12 [33] J. Lin, Z. W. Peng, C. S. Xiang, G. D. Ruan, Z. Yan, D. Natelson, J. M. Tour, *ACS*  
13 *Nano* **2013**, 7, 6001-6006.

- 1 [34] M. S. Park, G. X. Wang, Y. M. Kang, D. Wexler, S. X. Dou, H. K. Liu, *Angew. Chem.*  
2 *Int. Ed.* **2007**, 46, 750-753.
- 3 [35] Y. C. Jiao, D. D. Han, Y. Ding, X. F. Zhang, G. N. Guo, J. H. Hu, D. Yang, A. G. Dong,  
4 *Nature Commun.* **2015**, 6, 6420.
- 5 [36] R. Hu, D. Chen, G. Waller, Y. Ouyang, Y. Chen, B. Zhao, B. Rainwater, C. Yang, M.  
6 Zhu, M. Liu, *Energy Environ. Sci.* **2016**, 9, 595-603.
- 7 [37] J. Biener, S. Dasgupta, L. Shao, D. Wang, M. A. Worsley, A. Wittstock, J. R. I. Lee, M.  
8 M. Biener, C. A. Orme, S. O. Kucheyev, B. C. Wood, T. M. Willey, A. V. Hamza, J.  
9 Weissmüller, H. Hahn, T. F. Baumann, *Adv. Mater.* **2012**, 24, 5083-5087.
- 10 [38] C. X. Peng, Z. B. Wen, Y. Qin, L. Schmidt-Mende, C. Z. Li, S. H. Yang, D. L. Shi, J. H.  
11 Yang, *Chemsuschem* **2014**, 7, 777-784.
- 12 [39] D. Kang, Q. Liu, M. Chen, J. Gu, D. Zhang, *ACS Nano* **2016**, 10, 889-898.
- 13 [40] Y. Z. Su, S. Li, D. Q. Wu, F. Zhang, H. W. Liang, P. F. Gao, C. Cheng, X. L.  
14 Feng, *ACS Nano* **2012**, 6, 8349-8356.

- 1 [41] A. Jahel, C. M. Ghimbeu, L. Monconduit, C. Vix-Guterl, *Adv. Energy Mater.* **2014**, 4,  
2 1400025.
- 3 [42] B. Luo, T. F. Qiu, L. Hao, B. Wang, M. H. Jin, X. L. Li, L. J. Zhi, *J. Mater. Chem. A*  
4 **2016**, 4, 362-367.
- 5 [43] C. Guan, X. Wang, Q. Zhang, Z. Fan, H. Zhang, H. J. Fan, *Nano Lett.* **2014**, 14, 4852-  
6 4858.
- 7 [44] B. Huang, X. H. Li, Y. Pei, S. Li, X. Cao, R. C. Masse, G. Z. Cao, *Small* **2016**, 12,  
8 1945-1955.
- 9 [45] L. Xia, S. Q. Wang, G. X. Liu, L. X. Ding, D. D. Li, H. H. Wang, S. Z. Qiao, *Small* **2016**,  
10 12, 853-859.
- 11 [46] K. Zhao, L. Zhang, R. Xia, Y. Dong, W. Xu, C. Niu, L. He, M. Yan, L. Qu, L. S. Mai,  
12 *Small* **2016**, 12, 588-594.
- 13 [47] D. Deng, J. Y. Lee, *Chem. Mater.* **2008**, 20, 1841-1846.

- 1 [48] B. B. Jiang, C. Han, B. Li, Y. J. He, Z. Q. Lin, *ACS Nano* **2016**, 10, 2728–2735.
- 2 [49] S. P. Wu, C. P. Han, J. Iocozzia, M. J. Lu, R. Y. Ge, R. Xu, Z. Q. Lin, *Angew. Chem.*  
3 *Int. Ed.* **2016**, 55, 7898–7922.
- 4 [50] S. P. Wu, R. Xu, M. J. Lu, R. Y. Ge, J. Iocozzia, C. Han, B. Jiang, Z. Q. Lin, *Adv.*  
5 *Energy Mater.* **2015**, 5, 1500400.
- 6 [51] B. B. Jiang, Y. J. He, B. Li, S. Q. Zhao, S. Wang, Y.-B. He, Z. Q. Lin, *Angew. Chem.*  
7 *Int. Ed.* **2017**, 56, 1869–1872.
- 8 [52] H. Wu, G. Chan, J. W. Choi, I. Ryu, Y. Yao, M. T. McDowell, S. W. Lee, A. Jackson, Y.  
9 Yang, L. Hu, Y. Cui, *Nature Nanotech.* **2012**, 7, 310–315.
- 10 [53] J. Y. Huang, L. Zhong, C. M. Wang, J. P. Sullivan, W. Xu, L. Q. Zhang, S. X. Mao, N.  
11 S. Hudak, X. H. Liu, A. Subramanian, H. Fan, L. Qi, A. Kushima, J. Li, *Science* **2010**,  
12 330, 1515–1520.
- 13 [54] S. Chen, Y. L. Xin, Y. Y. Zhou, F. Zhang, Y. R. Ma, H. H. Zhou, L. M. Qi, *J. Mater.*  
14 *Chem. A* **2014**, 2, 15582–15589.

1 [55] S. Q. Zhao, Z. W. Wang, Y. J. He, B. B. Jiang, Y. W. Harn, X. Q. Liu, F. Q. Yu, F.

2 Feng, Q. Shen, Z. Q. Lin, *ACS Energy Lett.* **2017**, *2*, 111–116.

3  
4 **Supporting Information**

5 Additional characterizations, and performances tests.

6 Supporting Information is available from the Wiley Online Library or from the author.

7  
8  
9 **Acknowledgements**

10 This work was financially supported by National Natural Science Foundation (21273161,  
11 51671154), Natural Science Foundation of Shanghai (17ZR1447800), the Program for  
12 Professor of Special Appointment (Eastern Scholar) at Shanghai Institutions of Higher  
13 Learning, Shanghai Innovation Program (13ZZ026), Hundred Youth Talent Plan of Tongji  
14 University, the Fundamental Research Funds for the Central Universities, the National Key  
15 Research and Development Program of China (Grant No. 2016YFB0700404), and the  
16 International Joint Laboratory for Micro/Nano Manufacturing and Measurement  
17 Technologies.

18  
19 Received: ((will be filled in by the editorial staff))

20 Revised: ((will be filled in by the editorial staff))

21 Published online: ((will be filled in by the editorial staff))

22  
This article is protected by copyright. All rights reserved.

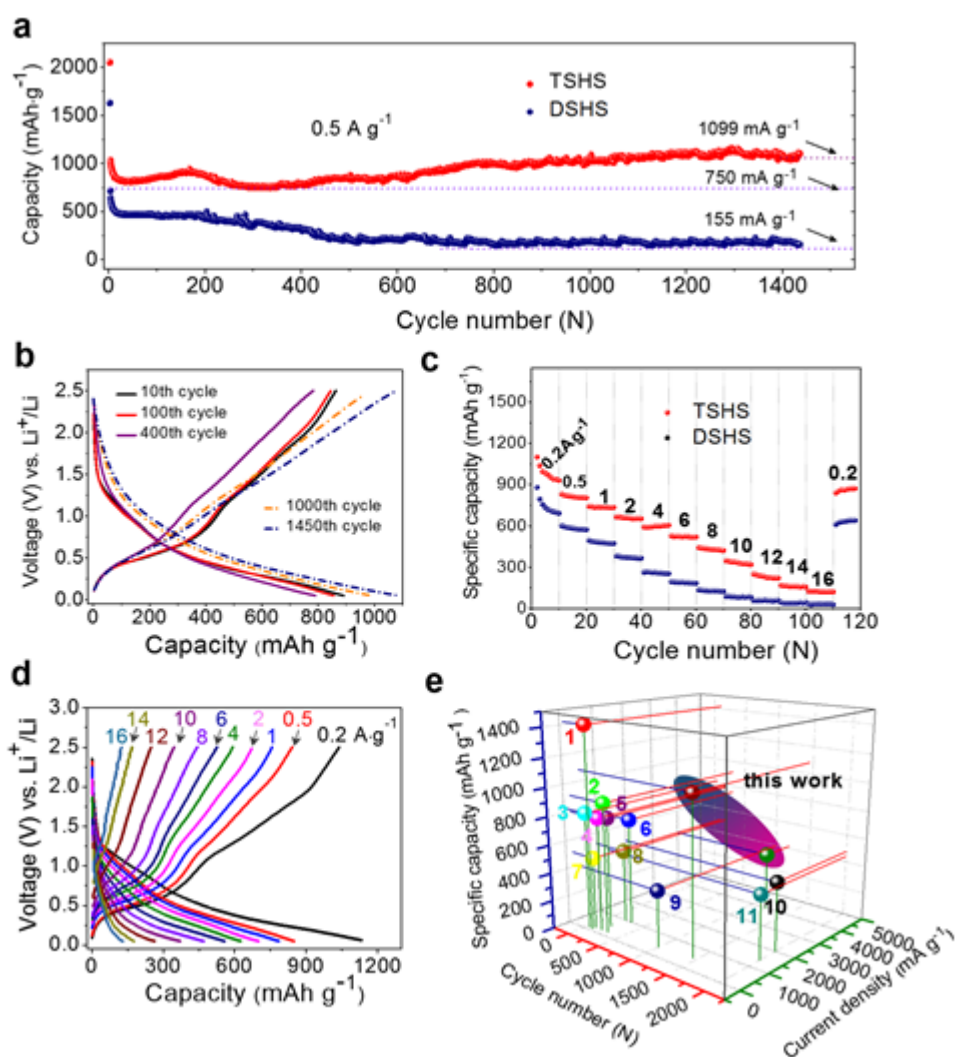


1 Figure 1. Synthetic route, and morphology and structure characterization for the TSHSs and  
2 DSHSs. a) Synthetic route for SnO<sub>2</sub> double-shelled hollow superstructure (DSHS) and  
3 Triple-shelled hollow superstructures (TSHS). b-d) SEM (b) and TEM (c-d) images of SnO<sub>2</sub>  
4 DSHSs. Inset in (d) is the high-resolution TEM image for an arbitrarily selected SnO<sub>2</sub>@C  
5 nanodot. e-g) SEM (e) and TEM (f-g) images of SnO<sub>2</sub> TSHSs. TEM image in (g)  
6 corresponds to the rectangle area in (f). Insets in (g) are magnified (right bottom) and high-  
7 resolution (upper right) TEM images showing the third shell assembled by SnO<sub>2</sub> nanorod  
8 arrays and single nanorod coated with few-layer graphene, respectively.

9

Author Manuscript

This article is protected by copyright. All rights reserved.

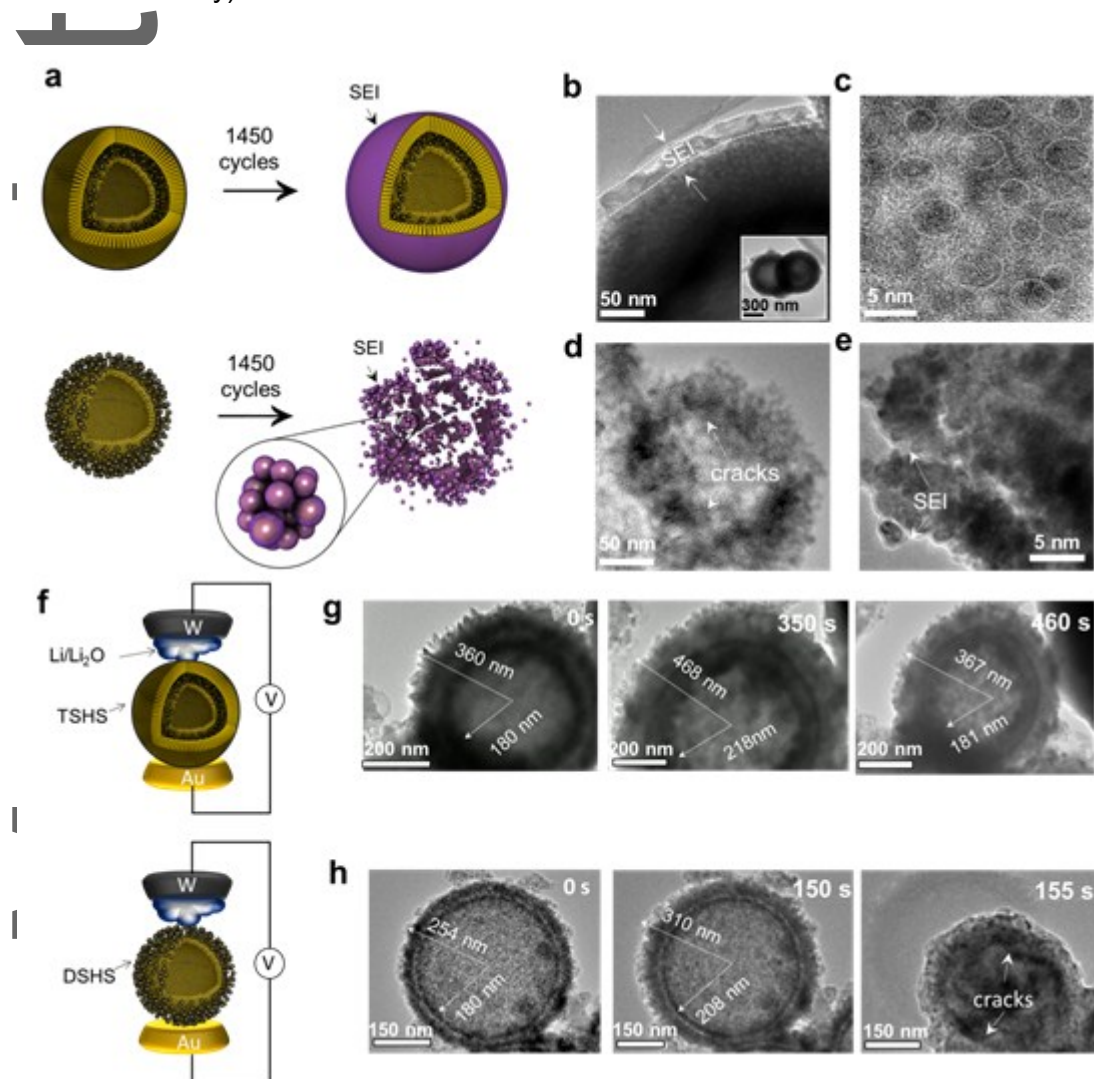


1

2 Figure 2. Battery performance of the TSHSs and the DSHSs. a) Cycling performance of the  
 3  $\text{SnO}_2$  DSHS and TSHS electrodes at  $0.5 \text{ A g}^{-1}$  between 2.5 and 0.05 V in coin-type half cells  
 4 at room temperature. b) Galvanostatic charge-discharge profiles of  $\text{SnO}_2$  TSHS electrode at  
 5 the 10th, 100th, 400th, 1000th, and 1450th cycle at  $0.5 \text{ A g}^{-1}$ . c) Rate capability of the  $\text{SnO}_2$   
 6 DSHS and TSHS electrodes at current densities between 0.2 and 16  $\text{A g}^{-1}$ , respectively. d)  
 7 Galvanostatic charge-discharge profiles of the  $\text{SnO}_2$  TSHS electrode at current densities

This article is protected by copyright. All rights reserved.

1 between 0.2 and 16 A g<sup>-1</sup>. e) Comprehensive performance comparison (specific capacity vs  
 2 cycle vs current density) of SnO<sub>2</sub> TSHS-based LIB with other SnO<sub>2</sub> anode-based LIBs.



3  
 4 Figure 3. Structure stability study of the TSHS and DSHS. a) Schematic illustration of final  
 5 architecture state of SnO<sub>2</sub> TSHS and DSHS upon lithiation/delithiation up to 1450 cycles. b-  
 6 c) Low- (b) and high-resolution (c) TEM images of a SnO<sub>2</sub> TSHS after 1450 cycles. d-e)  
 7 Low- (d) and high-resolution (e) TEM images of a SnO<sub>2</sub> DSHS after 1450 cycles. f)

This article is protected by copyright. All rights reserved.

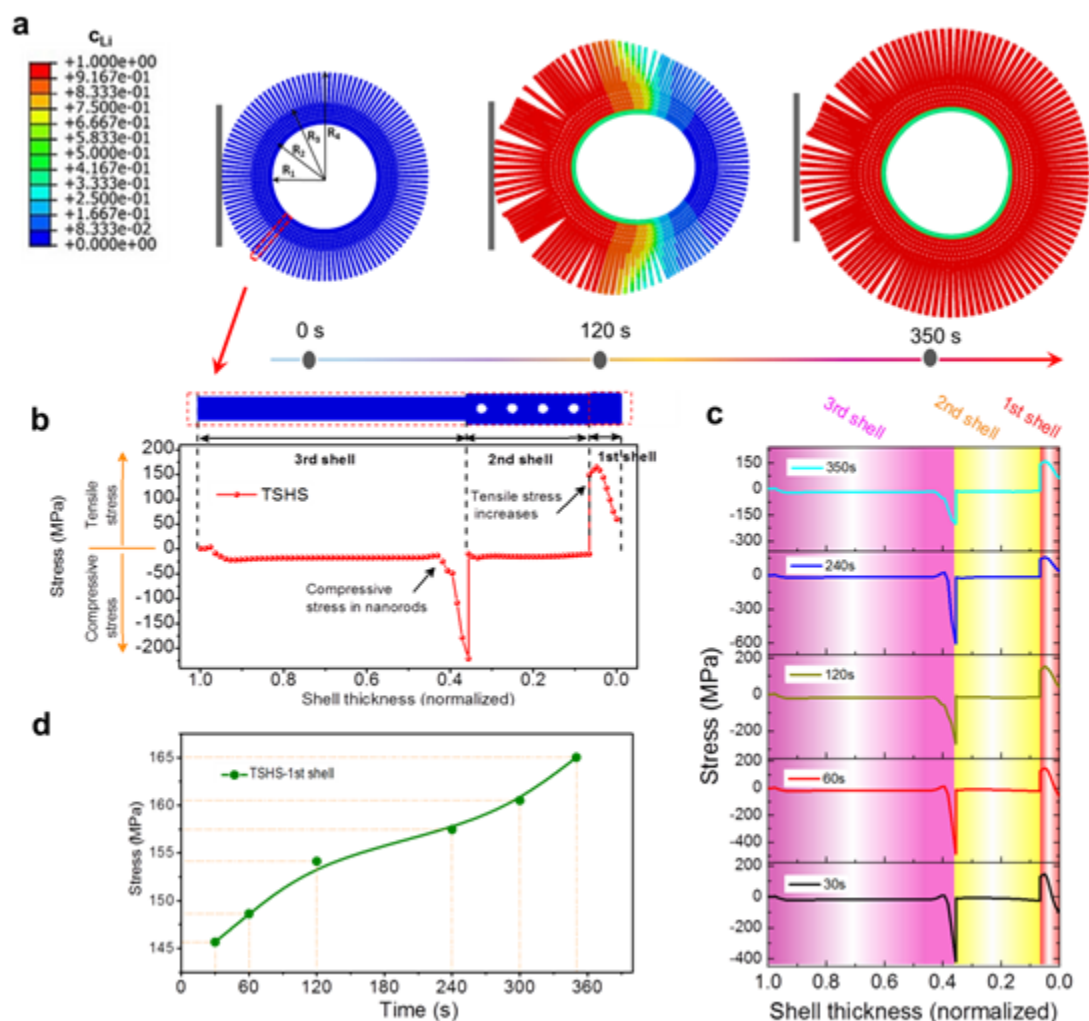
1 Schematic of the dry cells based on a SnO<sub>2</sub> TSHS and a DSHS for *in situ* TEM study. g-h)  
2 Time-lapse TEM images for a SnO<sub>2</sub> TSHS (g) and a DSHS (h) during a full lithiation-  
3 delithiation process with an applied voltage of  $\pm 3V$  between W and Au electrodes. Scale  
4 bars in g and h are 200 nm and 150 nm, respectively.

5

6

Author Manuscript

This article is protected by copyright. All rights reserved.



1

2 Figure 4. Mechanics simulations for the TSHS during lithiation process. a) Maximum  
 3 principal stress contours on deformed shapes of TSHS during lithiation at 0, 120 and 350 s.  
 4 Normalized Li concentration,  $c_{Li}$ , defined as the actual Li concentration divided by the Li  
 5 concentration in the fully lithiated state. The lithiation reaction front is located at the interface  
 6 between pristine (blue) and lithiated (red) phases. b) Evolution of stress in the three shells of  
 7 a TSHS after lithiation. The shell thickness, from the first shell to the third shell, is normalized

Author

This article is protected by copyright. All rights reserved.

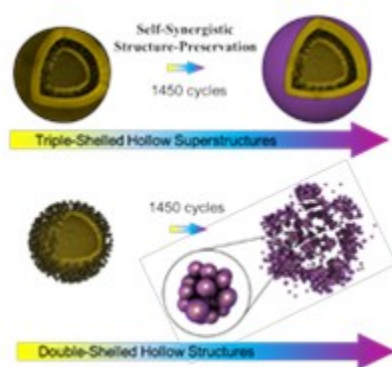
1 as 0 to 1. c) hoop stress evolution of the first, second and third shell of the TSHS during  
2 lithiation. d) the peak value of tensile stress in first shell as function of time.

3

4

5

6 Table of contents



7

SnO<sub>2</sub> triple-shelled hollow superstructures with a low carbon content (4.83%) can withstand a huge volume expansion of ~231.8% and deliver a high reversible capacity of 1099 mAh g<sup>-1</sup> even after 1450 cycles, due to their self-synergistic structure-preservation behavior that protects the superstructures from collapse and guarantees the electrode structural integrity during long-term cycling.

8

9

Auth

This article is protected by copyright. All rights reserved.



Minerva Access is the Institutional Repository of The University of Melbourne

**Author/s:**

Zu, L;Su, Q;Zhu, F;Chen, B;Lu, H;Peng, C;He, T;Du, G;He, P;Chen, K;Yang, S;Yang, J;Peng, H

**Title:**

Antipulverization Electrode Based on Low-Carbon Triple-Shelled Superstructures for Lithium-Ion Batteries

**Date:**

2017-09-13

**Citation:**

Zu, L., Su, Q., Zhu, F., Chen, B., Lu, H., Peng, C., He, T., Du, G., He, P., Chen, K., Yang, S., Yang, J. & Peng, H. (2017). Antipulverization Electrode Based on Low-Carbon Triple-Shelled Superstructures for Lithium-Ion Batteries. *ADVANCED MATERIALS*, 29 (34), <https://doi.org/10.1002/adma.201701494>.

**Persistent Link:**

<http://hdl.handle.net/11343/293095>